



Influence of surface pretreatment on porosity and microstructure of laser welding in AlSi10Mg alloys sheets fabricated by laser powder bed fusion

Can Wang¹ · Dingyong He^{1,2} · Li Cui¹ · Xingye Guo¹ · Zhen Tan¹ · Xu Wu¹

Received: 7 April 2023 / Accepted: 18 August 2023 / Published online: 29 August 2023
© International Institute of Welding 2023

Abstract

Surface pretreatment is of great significance for improving the welding quality of metal materials, especially aluminum alloys. At present, the welding process is introduced to join the laser powder bed fusion (LPBF) AlSi10Mg alloys or their repair during manufacturing or service. However, the high susceptibility of hydrogen pores is one of the most important problems encountered in the fusion welding process of LPBF AlSi10Mg alloys. To clarify the influence of the surface state of the base metal on the hydrogen pore characteristics, the LPBF AlSi10Mg sheets were pretreated by chemical cleaning treatment (CCT), mechanical polishing treatment (MPT), and chemical cleaning treatment after mechanical polishing treatment (MPT-CCT) before laser welding. Subsequently, the hydrogen pore characteristics, microstructure, and micro-hardness of the welded joints were investigated. The experimental results show that laser welding with MPT-CCT significantly reduces the porosity and pore diameter. In addition, MPT-CCT can eliminate most of the broken and discontinuous surface oxide film and Mg enrichment. In summary, the necessity of MPT-CCT for LPBF AlSi10Mg alloys is analyzed systematically, which is of great significance to improve the welding quality.

Keywords LPBF AlSi10Mg alloys · Surface pretreatment · Porosity · Microstructure · Mechanical properties

1 Introduction

Metal-based additive manufacturing (AM), which allows producing structural and functional parts employing a layer-by-layer addition of material starting from 3D digital models, is a potentially disruptive technology across multiple industries, including the aerospace, biomedical, and automotive industries [1]. In the past years, LPBF has been developed as an economically viable technology for fabricating complex geometries in aerospace industries and also as an advanced technique for component repairs [2–4].

However, due to the limit of the building chamber's available size and other factors, the dimension of the LPBF parts is small. As a result, welding may be necessary to meet industry needs for larger parts. Furthermore, repairing LPBF components by welding is more cost-effective and time-saving than replacing them, making welding technologies a practical solution [5–7]. Prashanth et al. [8], Du et al. [9], and Moeini et al. [10] employed friction welding (FW), a solid-state joining technique commonly used to join LPBF Al-12Si or AlSi10Mg parts, showing that the improvements in the joints' ductility were strongly related to a pronounced change in the Si-rich phases and the α -Al cells in the Al matrix. Nahmany et al. [11–13] investigated the electron beam welding (EBM) of LPBF AlSi10Mg workpieces and effectively applied this technique to produce a thin-walled pressure vessel. Biffi et al. [14] and Zhang et al. [15] investigated the laser weldability of LPBF AlSi10Mg alloy. Some investigations have studied the weldability of additive manufacturing parts, but the research on surface treatment before welding is still limited, as well as lower mechanical properties of the weld seam than the base metal (BM) and high susceptibility to hydrogen pores have not been resolved yet.

Recommended for publication by Commission I - Additive Manufacturing, Surfacing, and Thermal Cutting

✉ Li Cui
cuili@bjut.edu.cn

¹ Institute of Welding and Surface Engineering Technology, Faculty of Materials and Manufacturing, Beijing University of Technology, Beijing 100124, PR China

² Beijing Engineering Research Center of Eco-materials and LCA, Beijing 100124, PR China

It is well known that aluminum alloys require various surface pretreatment processes before welding in order to reduce the influence of surface oxide film. At the same time, the formation of pores in aluminum alloy welding is mainly due to the significant difference in the hydrogen solubility of aluminum in solid and liquid states [16]. The dense oxide film, impurities on the BM surface, and the filling material, adsorbing the crystalline water and chemical water from the air and shielding gas, are decomposed to produce hydrogen gradually. The precipitated hydrogen has no time to escape and remains to form pores in the weld seam. Thus, the powder of LPBF aluminum alloy has a larger surface in contact with the surroundings than a conventional forgeable piece or casting component; it offers more possibilities to absorb moisture from the environment. This moisture and hydrogen have been dissolved in the powder and cannot be completely eliminated during the additive manufacturing process. And for the AM parts, the sides and any areas in contact with the supporting material have a rougher surface. Therefore, it is necessary to perform surface pretreatment on the BM before welding to reduce the porosity and the associated surface imperfections.

Considering the pretreatment of aluminum alloys before welding, the effective cleaning of aluminum substrate can be achieved by a variety of processes. Laser welding with coatings, e.g., galvanized surfaces on steel, has been extensively studied for improving corrosion resistance [17]. It has been reported that the produced vapor from the coating can be entrapped, leading to variations in recoil pressure and so on, which might be similar to oxidized aluminum surfaces in this work. It is also known from there that oxide skins can lead to reactions in the melt pool. When laser welding with coatings, e.g., galvanized surfaces, similar effects might occur. Meanwhile, whether the surface pretreatment by using coatings is suitable for LPBF parts remains to be verified. At present, no detailed description of surface pretreatment of LPBF AlSi10Mg alloy has been reported based on the literature.

It is well known that when removing the aluminum oxide layer, there will be less disturbance in the process and, thus, less pores. The pores affected by the aluminum oxide layer usually are process pores, but not hydrogen pores. This is because the formation of the process pores in the weld seam is mainly attributed to the instability of the laser keyhole resulting from the recoil force of the vapor on the liquid metal when the laser power density is high enough [18]. However, the pores formed in the WM of LPBF AlSi10Mg alloy show standard circles with much smaller sizes, which can be determined as hydrogen pores. The formation mechanism of hydrogen pores in laser welding of LPBF AlSi10Mg alloys is similar to that in traditional Al-based alloys. The formation of hydrogen pores during the welding of conventional aluminum alloys is caused by the presence of moisture

or hydrogen in the welding environment, oxide film on the surface, and hydrogen generated by the decomposition of impurities, welding consumables, and BM itself [19]. It is generally thought that the weld pool will absorb hydrogen, and then supersaturated hydrogen rejects from the liquid metal to form bubbles during cooling and solidification due to a decrease in hydrogen solubility, especially a sharp drop at the solidification temperature between liquid and solid. If the bubbles cannot float out from the weld pool before solidification, they will remain in the weld as pores [20]. For the LPBF AlSi10Mg alloys, the reason for the high hydrogen porosity occurred in the WM was largely associated with the much higher amount of oxygen and hydrogen in the LPBF AlSi10Mg alloys than that of the casting ones, owing to the special powder characteristics, which are used to prepare the LPBF aluminum alloys, having a larger surface in contact with the surroundings than conventional forgeable or casting bulk materials [21, 22]. Beckmann et al. [23] reported that the hydrogen content in the LPBF part was seven times higher than that in the cast parts. Our previous study also has confirmed the high hydrogen content of the WM in the laser joint of LPBF AlSi10Mg alloys [24]. Therefore, it is of great significance in doing pretreatment for the surface of LPBF aluminum alloys before laser welding.

Compared with conventional aluminum alloy, welding of LPBF AlSi10Mg alloys has been particularly challenging [14]. Characteristics of laser welding include small beam size, precise control of beam shape and position, and very high energy density. The extension of the thermally affected areas is narrow with consequent low residual stresses and almost no distortions [20]. Using laser welding can improve the mechanical properties of LPBF Al-Si welded joints [15]. Prashanth et al. [8] had proposed that the pre-existing oxide films might cause pore formation in the weld seam of the LPBF Al-Si alloys. Large amounts of spherical porosities were generated because the dissolved hydrogen came from the oxide films covering powder or moisture. Different BM surface states still affect the absorptivity and the laser energy input into the weld seam, affecting the dilution ratio of BM into the weld seam [25]. Different dilution ratios affect the melting amount of BM as well as the hydrogen content in the melting pool [24]. Therefore, the study of surface pretreatment of the LPBF AlSi10Mg alloys is critical to the weld seam.

This paper investigated the effect of surface pretreatment on the porosity and microstructure properties of the welded joints that were carried out by autogenous laser welding of LPBF AlSi10Mg alloys. Specific microstructural analyses were investigated on LPBF AlSi10Mg specimens, followed by surface characterization at the microstructural scale to better understand the influence of surface pretreatment with LPBF AlSi10Mg alloy on welded joints.

2 Materials and experimental methods

2.1 Materials

The raw AlSi10Mg powder prepared by gas-atomized was employed for preparing the Base Material sheets in the present study. The size distribution of the powders was mainly in the range of 15–53 μm through Tod Laser Particle Sizer, and the chemical composition of the AlSi10Mg powders is shown in Table 1. The LPBF AlSi10Mg sheets for welding in the dimension of $60 \times 30 \times 3 \text{ mm}^3$ were fabricated by EOS M280 in a high-purity argon protection environment (99.99%). During the LPBF processing, the raw AlSi10Mg powders were deposited on an Al substrate, which was pre-heated to 150 °C. The oxygen content of less than 200 ppm was kept under argon gas protection. The laser scanning path of each layer was rotated 67° from the path of the previous layers. The LPBF process parameters were optimized by the orthogonal experiment for achieving a high relative density. The samples shown in Fig. 1, with a relative density of 99.6% for welding, were prepared with a laser power of 370 W, a scanning speed of 1300 mm/s, a hatching space of 0.19 mm, and a layer thickness of 20 μm . In this study, the relative density of as-built AlSi10Mg samples was estimated by the Image method using the Image J software. Considering that LPBF Al alloys produced with optimized parameters can achieve a relative density that exceeds 99%, the LPBF AlSi10Mg alloys prepared in this study have a comparatively high relative density.

As shown in Fig. 1, the macrostructure of the LPBF AlSi10Mg alloys in the side view at the Y-Z plane and X-Z plane parallel to the processing direction is similar, exhibiting a typical “fish-scale” pattern in the melt pool. The macrostructure in the top view at the X-Y plane perpendicular to the processing direction consists of columnar morphology with a width of approximately 100–200 μm but various lengths.

2.2 Surface pretreatment

Four types of surface pretreatment processes were prepared on the LPBF AlSi10Mg alloys before welding, including (1) untreated (UNT, the original state was only treated with acetone), (2) chemical cleaning treatment (CCT), (3) mechanical polishing treatment (MPT), and (4) their combination (chemical cleaning treatment after mechanical polishing treatment, MPT-CCT). In the MPT, the welding surface of the X-Z plane BM specimens was mechanically polished to remove about 0.5 mm thickness with the abrasive paper of 1000 meshes,

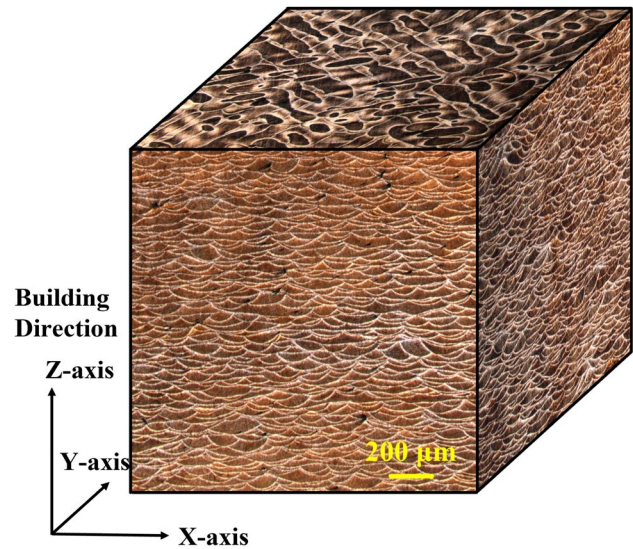


Fig. 1 Three-dimensional macrostructure of LPBF AlSi10Mg alloys

then washed away the surface particles. And the CCT applied to LPBF AlSi10Mg alloy specimens consists of an alkaline followed by an acid treatment. The CCT specimens were first soaked in an alkaline-saturated sodium hydroxide (NaOH) aqueous solution at 60 °C and then ultrasonically washed with deionized water and dried. Subsequently, the identical specimens were cleaned in a 30% nitric acid (HNO₃) aqueous solution. Finally, the specimens were ultrasonically cleaned with deionized water. The welding should be conducted within 24 h after the surface pretreatment.

2.3 Laser welding experimental

LPBF AlSi10Mg sheets in the dimension of $60 \times 30 \times 3 \text{ mm}^3$ were used for autogenous laser welding using a YLR-6000 fiber laser (IPG, Germany) with a wavelength of 1060–1070 nm and maximum output power of 6 kW, delivered in continuous wave mode through an output fiber core diameter of 100 μm . The laser beam was transmitted through a processing fiber with a diameter of 300 μm , collimated by a lens of 150 mm focal length, and then focused on the sheet surface by a focusing lens with 200 mm focal length. The laser beam was inclined 10° to the vertical direction to avoid equipment damage from beam reflection. The laser's spot size was approximately 0.3 mm when the beam was focused on the BM surface. The ultra-high-purity argon gas was used as the primary

Table 1 Chemical composition of the AlSi10Mg powders (wt.%)

Elements	Si	Mg	Fe	Mn	Cu	Ni	Zn	Ti	Pb	Sn	Al
Content	9–11	0.42	0.10	0.08	0.05	0.05	0.10	0.15	0.05	0.05	Bal.

shielding gas at a flow rate of 15 L/min to shield the welding pool from the surrounding atmosphere.

A schematic diagram of the autogenous laser welding process of LPBF AlSi10Mg alloys is illustrated in Fig. 2. The laser beam was focused on the X-Z plane, and the welding direction was perpendicular to the processing direction along the X-axis. To obtain a sound weld shape, the welding parameters were optimized as a laser power of 2200 W, a travel speed of 30 mm/s, and a defocused beam distance of 0 mm.

3 Characterization of microstructure and mechanical properties

After welding, the welded joints were cut transversely and longitudinally prepared for metallographic inspection by mounting, mechanical polishing, and etching in a Keller reagent (1 % HF + 1.5 % HCl + 2.5 % HNO₃ + 95 % H₂O) to display weld shapes and microstructures. The macrostructure of the welded joints and BM surface roughness were examined using a laser scanning confocal microscope (LSCM, Olympus, LEXT OLS4100). The porosity was calculated with the ratio of the pore areas to the whole weld area. The microstructure of the welded joints was examined using an optical microscope (OM) and scanning electron microscopy (SEM). An FMS300E micro-hardness tester

was employed for the hardness test, during which the load was fixed at 100 g, and the loading process lasted for 10 s. X-ray photoelectron spectroscopy (XPS) was conducted to characterize the oxide film. An ultra-high-resolution scanning electron microscopy-focused ion beam (SEM-FIB, Helios G4 PFIB CXe) was used to prepare ultra-thin section specimens for TEM (Titan-Themis) observation. For further refinement of the oxide layer analysis, the FIB specimen was prepared using a platinum (Pt) coating applied locally to the alloy surface to protect the oxide film in the region of interest on the surface from being damaged by the high-energy ion beam [26].

4 Results

4.1 The influence of surface pretreatment on the BM

Figure 3 depicts the 3D topographical images of the measured surface roughness parameters in terms of the arithmetic mean for the BM with the different surface pretreatment processes of UNT, CCT, MPT, and MPT-CCT. As indicated in Fig. 3, the surface from the UNT specimen suffered an uneven appearance with an average roughness Ra of 8.3 μm, presenting some bumps on the surface with UNT mainly caused by a stair-step effect, and the unmelted or partially

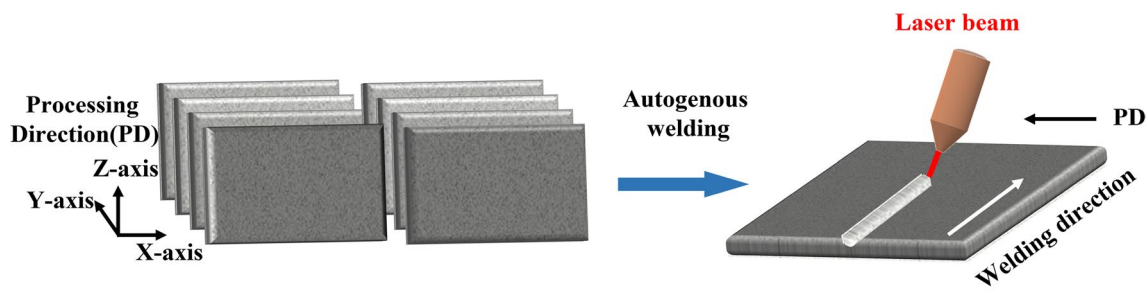


Fig. 2 Schematic diagram of autogenous laser welding setup of LPBF AlSi10Mg alloys

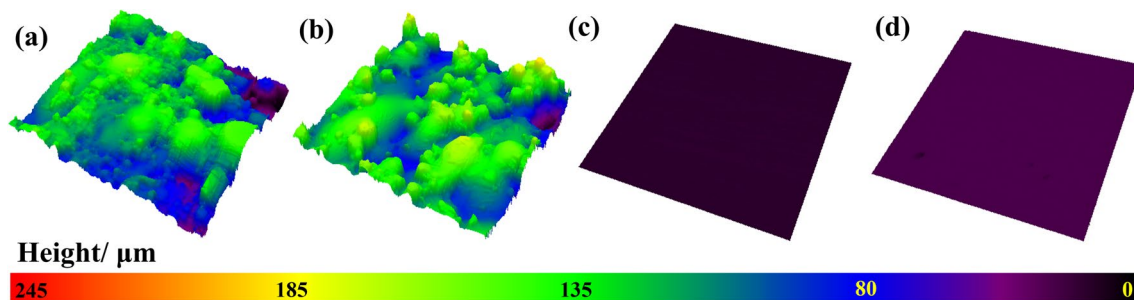


Fig. 3 Roughness and morphology of different surface states for LPBF AlSi10Mg specimens: (a) UNT, (b) CCT, (c) MPT, and (d) MPT-CCT

melted powders during LPBF processing. Generally, the powder materials introduce more surfaces and thus expose larger surfaces of Al alloys to oxygen, although the chamber was argon-shielded with only less than 0.2% oxygen. On the other hand, powder materials absorb more laser energy and achieve higher temperatures, making Al more sensitive to oxygen [27]. Therefore, the UNT specimen suffered the most severe oxidation among the four specimens. For the CCT specimen, the surface showed similar morphology with slightly decreased roughness R_a of $7.8 \mu\text{m}$. Thus, there was no obvious difference in surface roughness between the UNT and the CCT specimen, while the chemical cleaning dealt with the surface could reduce some of the oxidation films. This implies that the oxidation of the CCT specimen was less severe compared to the UNT specimen due to the more effective removal of the oxides by means of chemical cleaning. In the case of the MPT and MPT-CCT specimens, much flatter surfaces with much less and lower bumps were observed as a result of the mechanical polishing pretreatment. The surface roughness R_a of the MPT and MPT-CCT specimen was significantly decreased to $0.18 \mu\text{m}$ and $0.19 \mu\text{m}$, respectively. Therefore, MPT and MPT-CCT specimens revealed much smoother surfaces with noticeably reduced roughness, which implies less oxidation compared to the UNT and CCT specimens [27].

Typical surface morphologies of BM with different pretreatment processes are depicted in Fig. 4. As shown in Fig. 4a, the UNT specimen exhibited irregular surface features and poor surface quality. In the CCT specimen,

some surface defects were removed, with a few slight corrosion pits observed on the surface. Hence, the CCT specimen showed slightly lower surface roughness than the UNT specimen. A smoother surface and slight longitudinal machining marks were visible on the MPT specimen surface in Fig. 4c. After applying MPT-CCT, surface irregularities were removed, and the microstructure consisting of Al-Si eutectic networks was visible along the cell boundaries. Thus, MPT removed uneven pits and impurities on the surface and reduced the surface area contacted with the surrounding air, and MPT-CCT would further etch the surface.

Figure 5 shows the microstructures of the Y-Z plane cross-sectional close to surfaces obtained with four types of surface pretreatment processes. Where yellow-dotted lines mark the contour morphology of different surface pretreatment close to the BM surface, and the red circles mark the sub-grain cell consisting of α -Al and the eutectic Si network. Different surface pretreatment strongly affected the sub-grain sizes and the cell morphology close to the surface. The UNT specimen had the coarsest cells with an average size of $1.65 \mu\text{m}$. The CCT specimen exhibited a more uniform and smoother surface than the UNT one, with a cell size of about $1.28 \mu\text{m}$, as shown in Fig. 5b. In the case of the MPT specimen, the cellular networks near the surface were almost broken due to the shear loads caused by the MPT. As shown in Fig. 5d, the substrates of the MPT-CCT specimens were deeply etched, resulting in obviously wider etching areas. The cell sizes of the MPT and MPT-CCT specimens were $2.54 \mu\text{m}$ and $1.23 \mu\text{m}$, respectively. Thus, the BM with MPT-CCT achieved

Fig. 4 Surface morphologies of LPBF AlSi10Mg specimens in the side view with X-Z plane under different pretreatment processes: (a) UNT, (b) CCT, (c) MPT, and (d) MPT-CCT

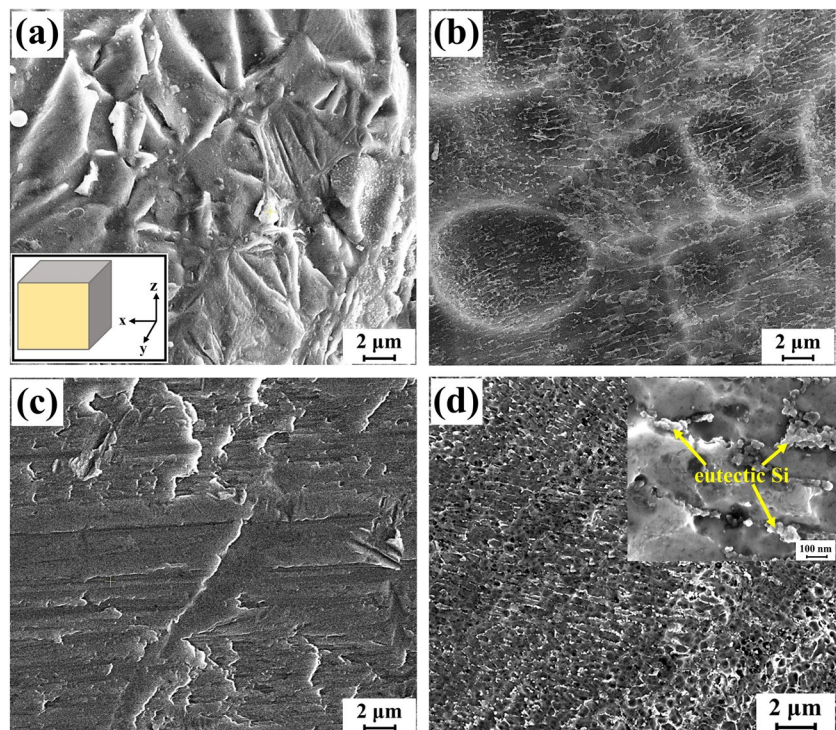
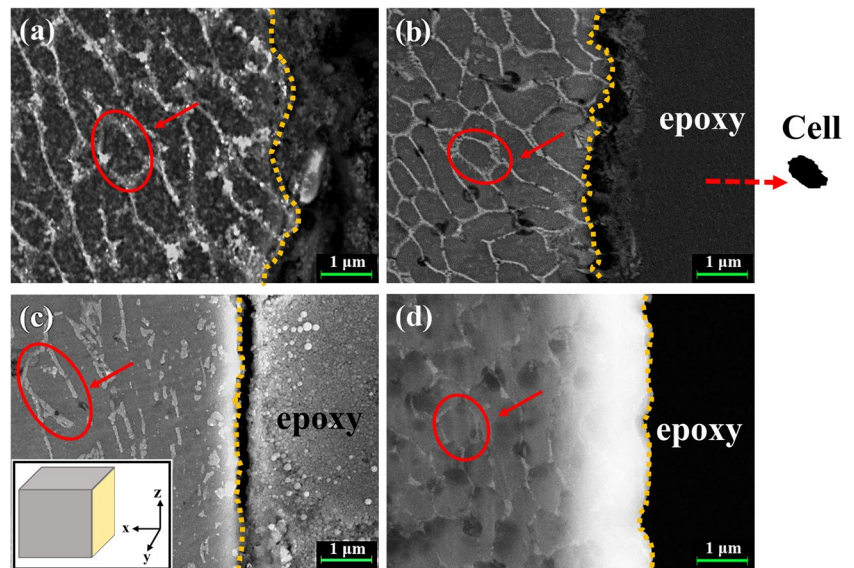


Fig. 5 SEM micrographs of the cross-section surfaces in the side view with the Y-Z plane of LPBF AlSi10Mg specimens with (a) UNT, (b) CCT, (c) MPT, and (d) MPT-CCT



finer sub-grain structures in the substrates than in the other pretreatment.

4.2 Weld shapes and pores

The cross-sections of welded joints with surface pretreatment are presented in Fig. 6a–e. The weld depths obtained with UNT, CCT, MPT, and MPT-CCT were 1.6 mm, 1.1 mm, 0.9 mm, and 0.8 mm, and the fusion areas of the weld seam were 2.04 mm², 1.64 mm², 1.04 mm², and 0.94 mm², respectively. The weld seam with UNT showed a higher weld penetration of depth and larger fusion area than that of the left ones. As shown in Fig. 6a₁–d₁, the longitudinal section profile of weld centers exhibited longitudinal weld morphology and porosity distribution. It proves that the pores distributed throughout the weld seam tended to aggregate at the upper part of the weld seam. The quantity of pores in each weld seam was determined by computing the mean outcomes of more than ten welding specimens. As shown in Fig. 6f, the porosity of the weld seams with the UNT, CCT, MPT, and MPT-CCT was 34.5 %, 14.6 %, 5.6 %, and 2.3 %, respectively. Thus, the porosity in the weld seam with CCT, MPT, and MPT-CCT on the BM surface was significantly decreased. The maximum pore diameters of the weld seam were qualified in Fig. 6f, and the maximum pore diameters were decreased from 554.92 to 49.62 μm. The macro-scale pores are completely disappeared in the weld seam with MPT and MPT-CCT, implying the key to reducing the welds' hydrogen pores was to select an appropriate surface pretreatment process.

Figure 7 shows the pore morphology of the weld center and the statistics of pore sizes. According to the difference in the diameters size of the pores, Fig. 7a–d show the main features of pores in four weld seams. In addition

to large hydrogen pores, there were still many tiny pores with red marks less than 10 μm in the weld seams. As shown in Fig. 7e, it was sub-divided into four groups: below 10 μm, 10~50 μm, 50~100 μm, and above 100 μm. The pore diameters less than 50 μm were predominately for four weld seams. And the statistical analysis showed that 15.84 % of the pore diameter of the UNT specimen had a size of more than 10 μm, and 18.66 % of these pore diameters were less than 10 μm. Accordingly, 1.47 % of the pore diameters of the MPT specimen had a size of more than 10 μm, which was reduced by 91.0 % compared with the UNT specimen. And 0.48 % of the MPT-CCT specimen had a size of less than 10 μm, which was reduced by 88.5 % compared with the UNT specimen. This indicated that the MPT and the MPT-CCT significantly reduced the number of pores more prominent than 10 μm generated in the weld seam.

4.3 Microstructure of the welded joints

Figure 8 shows microstructures in the cross-section of welded joints, taken from the fusion line (Fig. 8a–d) and the weld center (Fig. 8a₁–d₁). Each welded joint revealed a columnar morphology near the fusion line, while the equiaxed structures were formed in the weld center. The associated morphology of the sub-grains was affected by constitutional supercooling as well as the ratio of temperature gradient (G) to the rate of solid-liquid interface movement (R) [20]. The equiaxed fine-grain zone (EQZ) revealed spherical, with sizes of approximately 46.2 μm, 50.4 μm, 30.3 μm, and 38.1 μm, respectively. Additionally, it shows that the spherical hydrogen pores of the UNT welded joint near the fusion boundary were more numerous and larger, in the range of 3.15~19.95 μm in diameter, and few

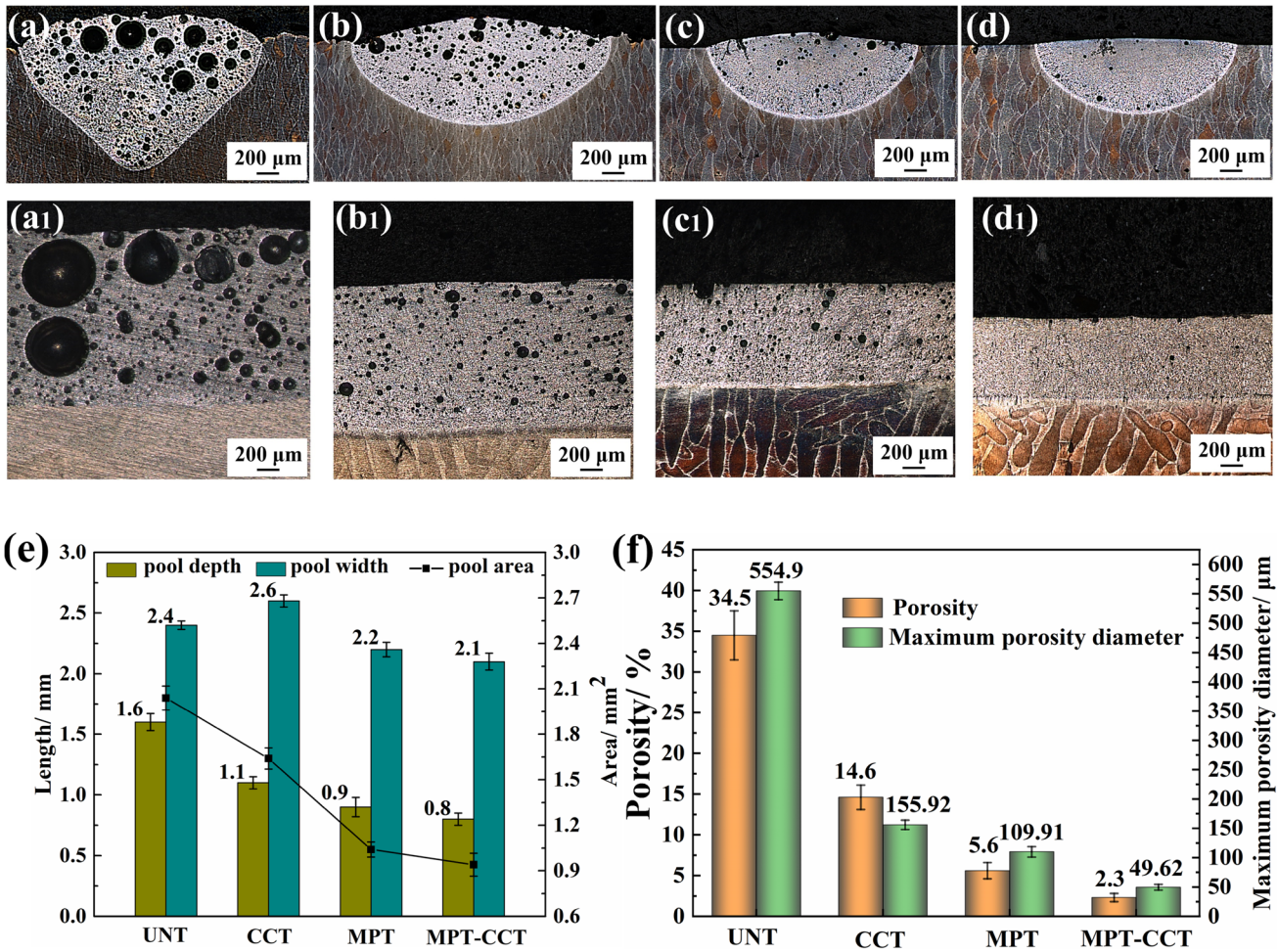


Fig. 6 Macrographs and longitudinal sections along the welding direction with (a, a₁) UNT, (b, b₁) CCT, (c, c₁) MPT, and (d, d₁) MPT-CCT; (e) pool depth, pool width, and pool area of laser welded joints; (f) the porosity and size of pores in the weld seam

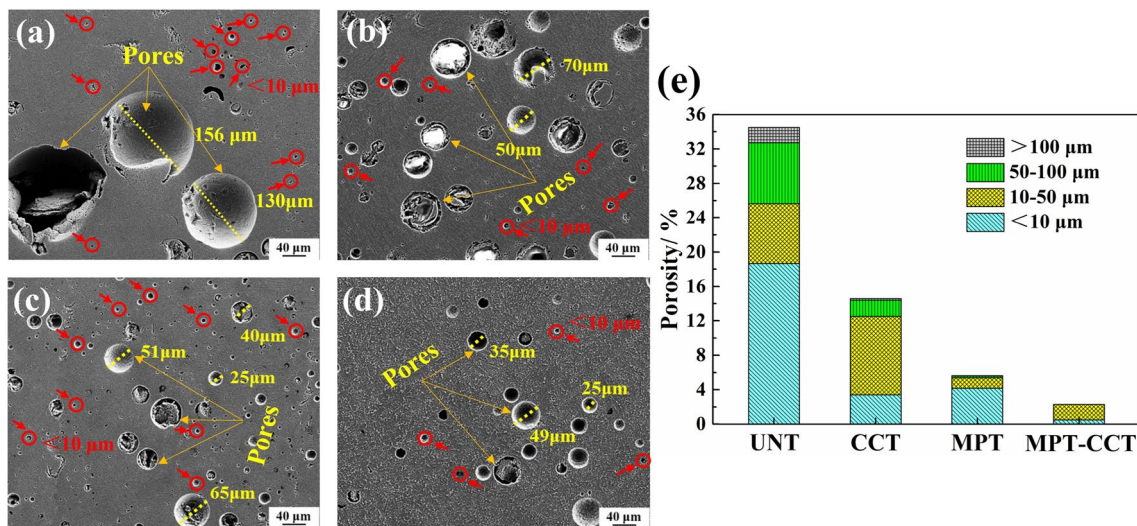


Fig. 7 The pores morphology in the weld seams with different surface pretreatment: (a) UNT, (b) CCT, (c) MPT, and (d) MPT-CCT; (e) the distribution of hydrogen pores

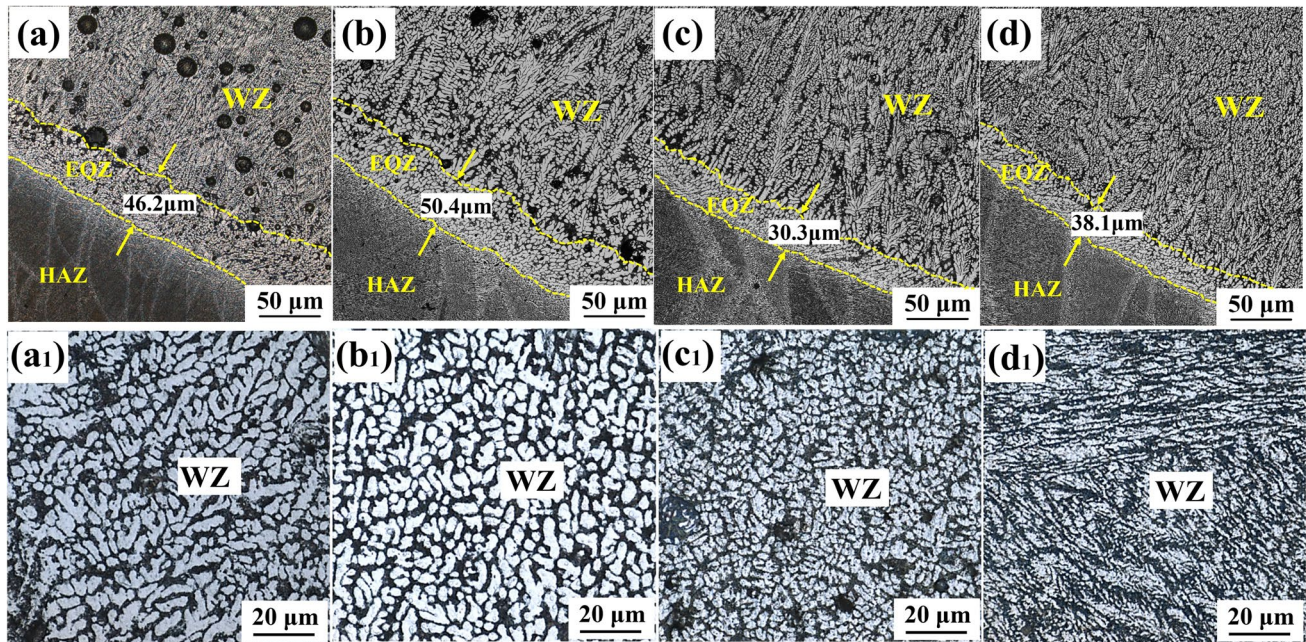


Fig. 8 Microstructures of LPBF AlSi10Mg welded joints in the cross-section: (a–d) near the fusion line and (a₁–d₁) in the welding center with UNT, CCT, MPT, and MPT-CCT, respectively

pores appeared in MPT and MPT-CCT welded joints. Figure 8a₁–c₁ exhibit that the cellular dendrite structures of the weld center were about 4.41 μm, 5.25 μm, and 3.58 μm. The dendritic structures formed in the MPT-CCT weld center were much finer than the other three specimens, as shown in Fig. 8d₁, because of high energy input and few heteronuclear points compared with the MPT weld seam.

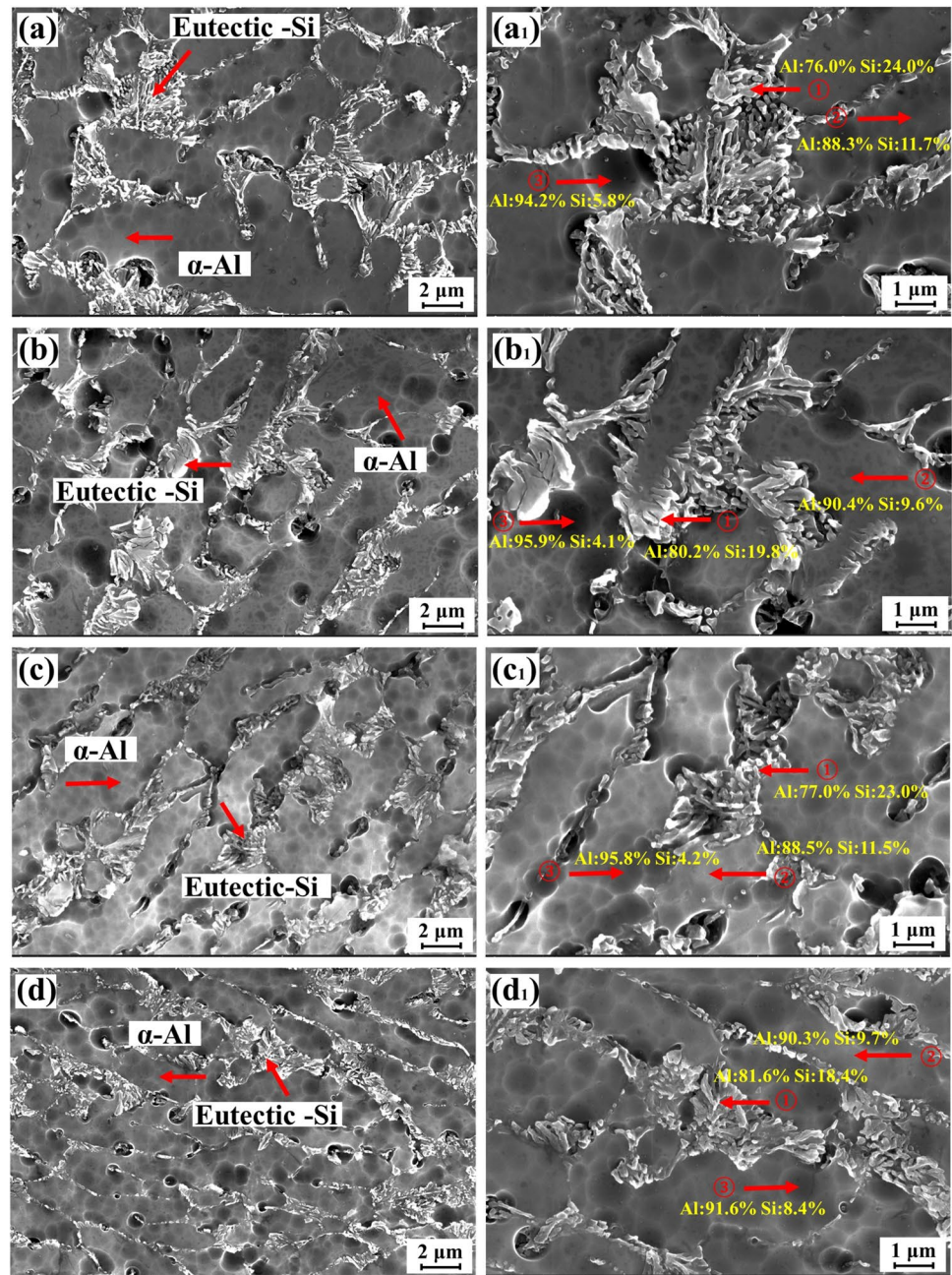
To further study the sub-grain structure, the SEM morphology of the weld seam was investigated, and the results are shown in Fig. 9. The dark zone corresponds to the Al matrix, enveloped by the white region that constitutes the Si-rich eutectic network. Still, some were elongated along the processing direction, indicating the thermal gradient direction. The average sizes of the α-Al cells in the weld seams with the UNT, CCT, MPT, and MPT-CCT were about 5.55 μm, 4.71 μm, 5.41 μm, and 4.29 μm, respectively. The size of the α-Al cells in the weld seam was much coarser than that of the LPBF AlSi10Mg alloy. The higher magnified micrograph in Fig. 9a₁–d₁ reveal that some rod-like or granular shape of Si-rich eutectic phases were distributed within the α-Al cell boundaries, having the length ranging from 0.75 to 4.75 μm (UNT), 0.60 to 3.00 μm (CCT), 0.45 to 2.85 μm (MPT), and 0.30 to 1.50 μm (MPT-CCT), respectively. Thus, the minimum size of α-Al cells and eutectic Si phases were obtained in the weld seam with MPT-CCT. As illustrated in circle 1 in the figures, the Si contents of the eutectic phases in the weld seam were increased to 24.0 wt%, 19.8 wt%, 23.0 wt%, and 18.4 wt% for the weld seams with the UNT, CCT, MPT, and MPT-CCT, respectively. The Si

contents in the Al matrix of the weld seam were 5.8 %, 4.1 %, 4.2 %, and 8.4 % from circle 3. The Si content of 8.4% in the Al matrix of the weld seam with the MPT-CCT was extremely close to the equilibrium (~10.0 wt%). Thus, it was beneficial to improve the effectiveness of the solid solution strengthening.

4.4 Micro-hardness distribution of the welded joints

A micro-hardness test was applied to the cross-sectional welded joints to investigate the mechanical performance. Figure 10 shows the profile of micro-hardness across from the top surface of the weld through the weld to the BM with the four specimens. It can be seen that the BM of LPBF AlSi10Mg alloys had an average micro-hardness value of 114.5 HV_{0.1}. For the welded joints, the micro-hardness in the weld seam region for the UNT, CCT, MPT, and MPT-CCT specimens was about 78.3 HV_{0.1}, 90.5 HV_{0.1}, 92.0 HV_{0.1}, and 105.2 HV_{0.1}, respectively. A reduced hardness was produced in the weld seam with the four specimens compared to the BM, showing a softening phenomenon occurred in the weld seam. However, the weld seam of the CCT, MPT, and MPT-CCT specimens exhibited higher hardness than that of the UNT specimen. This indicates that the pretreatment with CCT, MPT, and MPT-CCT effectively improved the hardness. Additionally, the weld seam of the MPT-CCT specimen showed the highest hardness up to 105.2HV_{0.1}, reaching 91.8% of the BM, which was higher than the other

Fig. 9 SEM micrographs of the microstructures of LPBF AlSi10Mg weld seams with UNT, CCT, MPT, and MPT-CCT: (a–d) cellular networks consisting of α -Al and eutectic Si phases; (a₁–d₁) high magnification of eutectic Si phases



specimens. The significantly improved hardness of the MPT-CCT specimen was attributed to the fine sub-grain structures and the solid solution strengthening of Si.

4.5 Surface oxide film

Figure 11 shows the TEM-EDS mapping of the elemental distribution of the FIB specimens (the sampling examples at the lower right corner) from different surface pretreatment of the BM surface. The TEM-EDS mapping of the UNT, CCT, MPT, and MPT-CCT surface clearly revealed the formation of the oxide film, ranging from 10 to 100 nm.

However, the thickness and the morphology of the oxide film for the four specimens were significantly different. The oxide film formed on the substrate in the UNT specimen has the largest thickness that contained two layers of an outer layer and an inner layer, as seen in Fig. 11a. The outer layer enriched in Al element was irregular and porous, while the inner layer on the substrate enriched in Mg element was much denser than that of the outer layer. The total thickness of the oxide film on the substrate with UNT was in the range of 68.6–113.2 nm, and the inner layer was about 32.8 nm. For the CCT, MPT, and MPT-CCT specimens, the outer layer of the oxide film formed in the UNT specimen

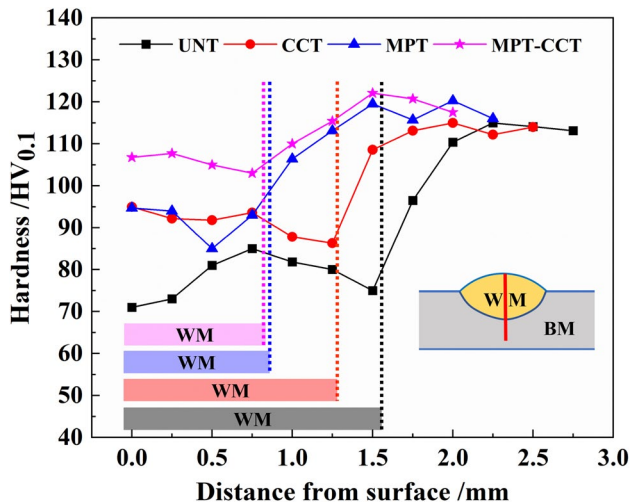


Fig. 10 Micro-hardness distribution of the cross-sectional welded joints with four specimens

completely disappeared, and only a thinner Mg-rich layer was observed on the substrate ranging from 9.4 to 15.2 nm, as shown in Fig. 11b–d. However, the MPT-CCT was conducted to further remove the partial inner layer. The surface changed unevenly due to the etch pits, where the oxygen enrichment layer became thinner, and the Mg element was uniformly distributed. The thickness of the broken and discontinuous oxide film on the surface of the MPT-CCT

specimen was about 5.23 nm. Thus, the BM with the MPT-CCT surface pretreatment significantly removed most of the surface oxide film.

A benchmark for the TEM-XPS method was jointly used in this work [28]. When X-ray impinges on the aluminum surface, the binding energy of oxide and the metallic species are separated by a few electron volts (eV), so it is possible to distinguish the contribution from both oxide and metal photoelectrons. The atomic contents of the elements in the surfaces of the MPT-CCT BM were tested using XPS, as shown in Fig. 12a. Al, Si, Mg, and O atomic contents were 14.29 %, 6.09 %, 2.62 %, and 27.08 %, respectively. As shown in Fig. 12b, the characteristic peaks of Al 2p in aluminum oxide (+3) and aluminum metal (0) were 74.87 eV and 72.87 eV (i.e., the chemical shift is 2.00 eV), respectively. According to the research of Strohmeier [29], the thickness of the oxide film can be estimated from the peak intensity difference between both Al 2p signals in the spectrum using the following calculation formula (1):

$$d_{\text{XPS}}(\text{nm}) = \lambda_o \cdot \sin\theta \cdot \ln \left(\frac{N_m \cdot \lambda_m \cdot I_o}{N_o \cdot \lambda_o \cdot I_m} + 1 \right) \quad (1)$$

where d_{XPS} is the calculated thickness of the oxide film, and θ is the emergence angle of the photoelectron. λ_o and λ_m , N_o and N_m , and I_o and I_m are the inelastic mean free path (IMFP), aluminum atomic volume density, and the

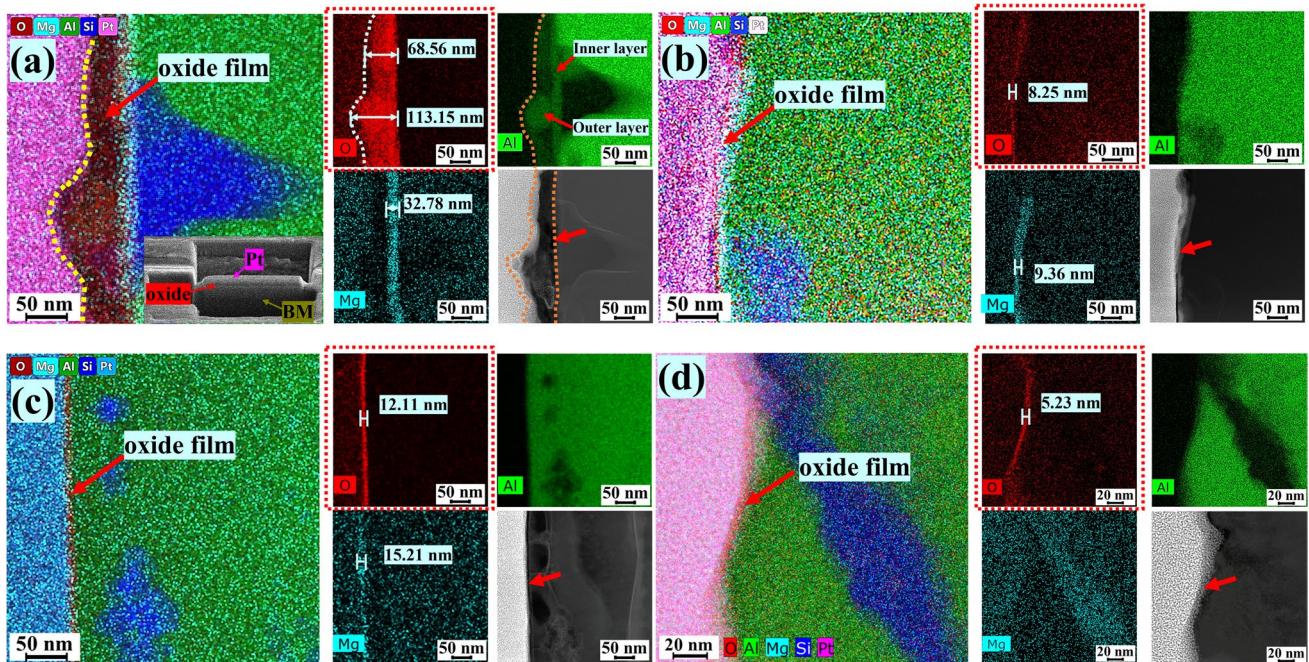


Fig. 11 TEM images and elemental mapping for BM with different surface pretreatment processes: (a) UNT, (b) CCT, (c) MPT, and (d) MPT-CCT

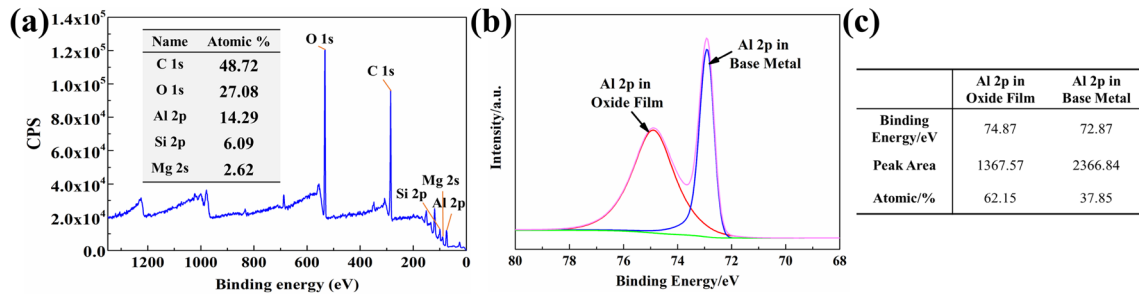


Fig. 12 Analysis of XPS patterns on the oxide film of the MPT-CCT: (a) broad scan spectra, (b) the characteristic peaks of Al 2p, and (c) statistical analysis of both peaks

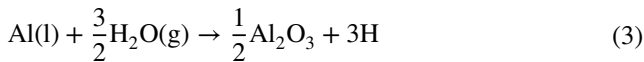
signal concentration ratios of Al 2p in the oxide film and BM, respectively. With reference to the literature, the values of λ_o , λ_m , and N_o/N_m used are 2.80 nm, 2.60 nm, and 1.6, respectively [30, 31]. In this experiment, $\theta = 90^\circ$. Besides, as shown in Fig. 12c, I_o and I_m were 62.15 % and 37.85 %, respectively. Therefore, the thickness of the oxide film was calculated to be 3.46 nm, and the result was basically consistent with the TEM above.

5 Discussion

Based on the above results and founding, a model for the influence of the BM surface states on the porosity of welded joint is illustrated in Fig. 13. The oxide film and impurities entered the molten pool when the UNT BM was heated by the laser. The crystalline water, chemical water from the air and shielding gas, and the oxide film on the AlSi10Mg alloy surface were decomposed gradually. The decomposed water was decomposed directly in the high-temperature region to produce hydrogen (H) [32]:



It could also react with the aluminum solution to form H:

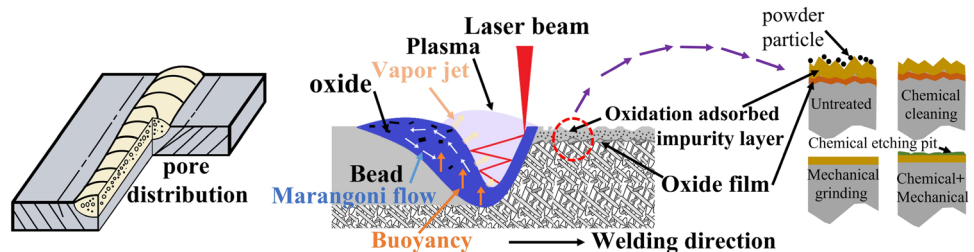


Due to the presence of impurities in the melt pool of UNT BM, the Marangoni convection was reversed, which circulated inward and downward, hindering hydrogen bubbles in the escape process [33–35]. At the same time, the oxide film and impurities affected the viscous force of the liquid metal [36]. The viscosity of the UNT specimen molten pool was increased, slowing down the floating of the bubbles. The pores did not have time to escape entirely and were accumulated close to the surface, thus increasing the tendency of big pores and higher porosity. The maximum pore diameter of the UNT weld seam was 554.92 μm .

Compared with the UNT weld seam, the large pores and porosity of the weld seam with CCT were decreased due to removing impurities, powder particles, and part of the oxide film on the surface. Strong melt fluidity promoted the large bubbles to float and escape during the welding process. In addition, after welding, the micro-pores in LPBF parts were released due to remelting and, combined with other micro-pores, grew up and floated. With the solidification of the molten pool, they remained in the weld seam. Thus, the CCT weld seam reduced porosity with more than 100 μm and 50–100 μm of pore diameters.

However, the porosity of the MPT weld seam was reduced by 61.6 % more than that of the CCT one. The BM surface had a big difference in the roughness between the CCT and MPT surfaces, resulting in the difference in laser absorptivity. Then, the fusion area of the MPT weld seam was reduced to 1.04 mm², which was 36.6% lower than that of the CCT weld seam. Thus, the lower amount of H was entrained in the molten pool from the

Fig. 13 Mechanism of the surface pretreatment of the BM on the formation of the pores in the welded joints



BM with the MPT. At the same time, due to the high roughness of the surface, the MPT surface had a small contact area with air, shielding gas, and laser beam during the welding process. Few wrapped gas and impurities were entrapped in the molten pool. Both resulted in decreased porosity and pore diameters, especially when the pore size was 10–50 μm .

The MPT-CCT weld seam exhibited a smaller fusion area than that of the MPT weld seam. It reduced the thickness of the surface oxide film, enlarged the Marangoni flow, and weakened the reverse flow of Marangoni convection, which led to the decrease of fusion area. The broken oxide film also made it easier for the pores to escape completely. And a lower amount of hydrogen was entrained in the molten pool of the MPT-CCT weld seam. Finally, the sizeable Marangoni convection promoted the escape of pores, and the Marangoni flow can also help to distribute the heat more evenly, reducing the likelihood of localized overheating and the formation of additional pores. And then, the MPT-CCT weld seam had the lowest porosity and diameter pores. The pore reduction was probably caused by the removal of the aluminum oxide film and reduced MgO layer based on Fig. 11 [36]. In summary, the MPT-CCT of LPBF aluminum alloy parts was of great significance to improve the welding quality.

6 Conclusions

Four different surface pretreatment processes of the LPBF AlSi10Mg sheets were prepared before welding to understand the influence of the surface pretreatment on the hydrogen pores and mechanical properties in the welded joints. The detailed surface morphology of the BM with four treatment states and the welds' porosity, microstructure, and micro-hardness were studied. The main conclusions are as follows.

- (1) The pretreatment of CCT, MPT, and MPT-CCT before welding effectively reduced both the porosity and the pore size compared to the UNT specimen. The porosity was significantly reduced to 2.3 % in the weld seam with the MPT-CCT.
- (2) The weld seam produced with the MPT-CCT exhibited a dendritic sub-structure with finer dendrites, while other specimens displayed an equiaxed sub-structure. The microstructure of the weld seam produced by the MPT-CCT specimen reveals a more uniform Si element distribution than that of the other specimens, close to the equilibrium value (~ 10.0 wt%) of AlSi10Mg, which improved the degree of the solid solution strengthening.
- (3) The weld seam of the MPT-CCT specimen showed the highest micro-hardness up to 105.2 HV_{0.1}, reaching 91.8% of the BM, which was higher than the

other specimens. The significantly improved hardness of the MPT-CCT specimen was attributed to the fine sub-grain structures and the solid solution strengthening of Si.

- (4) The broken and discontinuous oxide film was about 3.46–5.23 nm with the UNT, CCT, and MPT specimens, while no Mg enrichment appeared in the MPT-CCT specimen. The pretreatment of the MPT-CCT specimen significantly removed most of the oxide film.
- (5) The increase of oxides and pollutants on the weld surface will increase the viscosity of the weld pool metal at high temperatures, reduce the fluidity, increase the surface tension, and increase the reverse flow of Marangoni convection, which circulated inward and downward, hindering hydrogen bubbles in the escape process. The MPT-CCT reduced the thickness of the surface oxide film, enlarged the Marangoni flow, weakened the reverse flow of Marangoni convection, and reduced the porosity of the weld seam.

Author contribution Can Wang: methodology, formal analysis, writing - original draft. Dingyong He: resources, writing - review and editing, funding acquisition. Li Cui: conceptualization, formal analysis, writing - review and editing. Xingye Guo: conceptualization, writing editing. Zhen Tan: validation, supervision. Xu Wu: methodology.

Funding This work was supported by the National Natural Science Foundation of China (grant number 52271018) and the National Key Research and Development Program of China (grant number 2021YFB3704205).

Data availability The raw/processed data required to reproduce these findings cannot be shared at this time as the data also forms part of an ongoing study.

Declarations

Competing interests The authors declare no competing interests.

References

1. Zhao C, Parab ND, Li X, Fezzaa K, Sun T (2020) Critical instability at moving keyhole tip generates porosity in laser melting. *Science* 370:1080–1086. <https://doi.org/10.1126/science.abd1587>
2. Hopkinson N, Hague R, Dickens PM (2006) Rapid manufacturing: an industrial revolution for the digital age. John Wiley & Sons, Ltd, New Jersey
3. Gu DD, Meiners W, Wissenbach K, Poprawe R (2013) Laser additive manufacturing of metallic components: materials, processes and mechanisms. *Int Mater Rev* 57:133–164. <https://doi.org/10.1179/1743280411Y.0000000014>

4. Debroy T, Wei HL, Zuback J, Mukherjee T, Zhang W (2018) Additive manufacturing of metallic components—process, structure and properties. *Prog Mater Sci* 92:112–224. <https://doi.org/10.1016/j.pmatsci.2017.10.001>
5. Martin JH, Yahata BD, Hundley JM, Mayer JA, Schaedler TA, Pollock TM (2017) 3D printing of high-strength aluminium alloys. *Nature* 549:365–379. <https://doi.org/10.1038/nature23894>
6. Aboulkhair NT, Maskery I, Tuck C (2016) The microstructure and mechanical properties of selectively laser melted AlSi10Mg: the effect of a conventional T6-like heat treatment. *Mater Sci Eng A* 667:139–146. <https://doi.org/10.1016/j.msea.2016.04.092>
7. Xiong ZH, Liu SL, Li SF, Yang YF, Misra R (2019) Role of melt pool boundary condition in determining the mechanical properties of selective laser melting AlSi10Mg alloy. *Mater Sci Eng A* 740:148–156. <https://doi.org/10.1016/j.msea.2018.10.083>
8. Prashanth KG, Damodaram R, Scudino S, Wang Z, Rao KP, Eckert J (2014) Friction welding of Al-12Si parts produced by selective laser melting. *Mater Des* 57:632–637. <https://doi.org/10.1016/j.matdes.2014.01.026>
9. Du Z, Chen HC, Ming JT, Bi G, Chua CK (2018) Investigation of porosity reduction, microstructure and mechanical properties for joining of selective laser melting fabricated aluminium composite via friction stir welding. *J Manuf Process* 36:33–43. <https://doi.org/10.1016/j.jmapro.2018.09.024>
10. Moeini G, Sajadifar SV, Wegener T, Brenne F, Böhm S (2019) On the low-cycle fatigue behavior of friction stir welded Al-Si12 parts produced by selective laser melting. *Mater Sci Eng A* 764:138189. <https://doi.org/10.1016/j.msea.2019.138189>
11. Nahmany M, Hadad Y, Aghion E, Stern A, Frage N (2019) Microstructural assessment and mechanical properties of electron beam welding of AlSi10Mg specimens fabricated by selective laser melting. *J Mater Process Technol* 270:228–240. <https://doi.org/10.1016/j.jmatprotec.2019.02.025>
12. Nahmany M, Stern A, Aghion E, Frage N (2017) Structural properties of EB-welded AlSi10Mg thin-walled pressure vessels produced by AM-SLM technology. *J Mater Eng Perform* 26:4813–4821. <https://doi.org/10.1007/s11665-017-2953-7>
13. Nahmany M, Rosenthal I, Benishti I, Frage N, Stern A (2015) Electron beam welding of AlSi10Mg workpieces produced by selected laser melting additive manufacturing technology. *Addit Manuf* 8:63–70. <https://doi.org/10.1016/j.addma.2015.08.002>
14. Biffi CA, Fiocchi J, Tuissi A (2019) Laser weldability of AlSi10Mg alloy produced by selective laser melting: microstructure and mechanical behavior. *J Mater Eng Perform* 28:6714–6719. <https://doi.org/10.1007/s11665-019-04402-7>
15. Zhang C, Bao Y, Zhu H, Nie X, Zeng X (2019) A comparison between laser and TIG welding of selective laser melted AlSi10Mg. *Opt Laser Technol* 120:105696. <https://doi.org/10.1016/j.optlastec.2019.105696>
16. Wang YJ, Yang JH (2020) Effect of surface treatment on bonding mechanical properties of aluminum alloy 6063. *Weld Technol* 49:8. <https://doi.org/10.13846/j.cnki.cn12-1070/tg.2020.01.005>
17. Shibli SMA, Meena BN, Remya R (2015) A review on recent approaches in the field of hot dip zinc galvanizing process. *Surf Coat Technol* 262:210–215. <https://doi.org/10.1016/j.surfcoat.2014.12.054>
18. Zhang XY, Huang T, Yang WX, Xiao RS, Liu Z (2016) Microstructure and mechanical properties of laser beam-welded AA2060 Al-Li alloy. *J Mater Process Technol* 237:301–308. <https://doi.org/10.1016/j.jmatprotec.2016.06.021>
19. Zhao YQ, Zhou XD, Liu T, Kang Y, Zhan XH (2020) Investigate on the porosity morphology and formation mechanism in laser-MIG hybrid welded joint for 5A06 aluminum alloy with Y-shaped groove. *J. Mater. Process.* 57:847–856. <https://doi.org/10.1016/j.jmapro.2020.07.044>
20. Zuo TC (2008) Laser materials processing of high strength aluminium alloys. National Defense Industry Press, Beijing
21. Aboulkhair NT, Simonelli M, Parry L, Ashcroft I, Tuck C (2019) 3D printing of aluminium alloys: additive manufacturing of aluminium alloys using selective laser melting. *Prog Mater Sci* 106:100578. <https://doi.org/10.1016/j.pmatsci.2019.100578>
22. Yang TY, Cui L, He DY, Huang H (2022) Enhancement of microstructure and mechanical property of AlSi10Mg-Er-Zr alloys fabricated by selective laser melting. *Acta Metall Sin* 58(9):1108–1117. <https://doi.org/10.11900/0412.1961.2021.00085>
23. Beckmann F, Emmelmann C (2019) Optimization of the weldability of laser additive manufactured aluminum by means of hydrogen minimization in the component and welding parameter optimization. In: Proceedings of Lasers in Manufacturing Conference. https://www.wlt.de/lim/Proceedings2019/data/PDF/Contribution_327_final.pdf
24. Cui L, Peng ZB, Chang YQ, He DY, Cao Q (2022) Porosity, microstructure and mechanical property of welded joints produced by different laser welding processes in selective laser melting als10mg alloys. *Opt Laser Technol* 150:107952. <https://doi.org/10.1016/j.optlastec.2022.107952>
25. Liu B, Wang CM, Mi GY, Wang J, Zhang W (2021) Oxygen content and morphology of laser cleaned 5083 aluminum alloy and its influences on weld porosity. *Opt Laser Technol* 140:107031. <https://doi.org/10.1016/j.optlastec.2021.107031>
26. Townsend A, Senin N, Blunt L, Leach RK, Taylor JS (2016) Surface texture metrology for metal additive manufacturing: a review. *Precis Eng* 46:34–47. <https://doi.org/10.1016/j.precisioneng.2016.06.001>
27. Yu WH, Sing SL, Chua CK, Tian XL (2019) Influence of re-melting on surface roughness and porosity of AlSi10Mg parts fabricated by selective laser melting. *J Alloy Compd* 792:574–581. <https://doi.org/10.1016/j.jallcom.2019.04.017>
28. Zhang Q, Huang M, Lv T, Lou M, Li Y (2020) Effect of surface treatments and storage conditions on resistance spot weldability of aluminum alloy 5182. *J Manuf Process* 58:30–40. <https://doi.org/10.1016/j.jmapro.2020.08.002>
29. Strohmeier BR (2010) An ESCA method for determining the oxide thickness on aluminum alloys. *Surf Interface Anal* 15:51–56. <https://doi.org/10.1002/sia.740150109>
30. Alexander MR, Thompson GE, Zhou X, Beamson G, Fairley N (2010) Quantification of oxide film thickness at the surface of aluminium using XPS. *Surf Interface Anal* 34:485–489. <https://doi.org/10.1002/sia.1344>
31. Viroulaud R, Swiatowska J, Seyeux A, Zanna S, Tardelli J, Marcus P (2017) Influence of surface pretreatments on the quality of trivalent chromium process coatings on aluminum alloy. *Appl Surf Sci* 423:927–938. <https://doi.org/10.1016/j.apsusc.2017.06.246>
32. Wang LL, Wang GW, Dong H, Ye MH, Li XY, Liu L, Pan JL, Ye ZY (2022) Plasma electrolytic oxidation coatings on additively manufactured aluminum-silicon alloys with superior tribological performance. *Surf Coat Technol* 435:128246. <https://doi.org/10.1016/j.surfcoat.2022.128246>
33. Han Y, Zhang Y, Jing H, Lin D, Xin P (2020) Selective laser melting of low-content graphene nanoplatelets reinforced 316L austenitic stainless steel matrix: strength enhancement without affecting ductility. *Addit Manuf* 34:101381. <https://doi.org/10.1016/j.addma.2020.101381>

34. Zhang DY, Zhang PD, Liu Z, Feng Z, Wang CJ, Guo YW (2018) Thermofluid field of molten pool and its effects during selective laser melting (SLM) of Inconel 718 alloy. *Addit Manuf* 21:567–578. <https://doi.org/10.1016/j.addma.2018.03.031>
35. Wang ZY, Zhuo LC, Yin EH, Zhao Z (2021) Microstructure evolution and properties of nanoparticulate SiC modified AlSi10Mg alloys. *Mater Sci Eng A* 808:140864. <https://doi.org/10.1016/j.msea.2021.140864>
36. Bao L, Li K, Zheng JY, Zhang YL, Zhan K, Yang Z, Zhao B, Ji VC (2022) Surface characteristics and stress corrosion behavior of AA 7075-T6 aluminum alloys after different shot peening processes. *Surf*

Coat Technol 440:128481. <https://doi.org/10.1016/j.surfcoat.2022.128481>

Publisher's note Springer Nature remains neutral with regard to jurisdictional claims in published maps and institutional affiliations.

Springer Nature or its licensor (e.g. a society or other partner) holds exclusive rights to this article under a publishing agreement with the author(s) or other rightsholder(s); author self-archiving of the accepted manuscript version of this article is solely governed by the terms of such publishing agreement and applicable law.